J. Fluid Mech. (2004), *vol.* 500, *pp.* 211–237.
DOI: 10.1017/S002211200300716X Printed in the United Kingdom

Experimental and numerical investigation of an O_2/NO supersonic free jet expansion

By A. BROC[1]†, S. DE BENEDICTIS[1]‡, G. DILECCE[1], M. VIGLIOTTI[1], R. G. SHARAFUTDINOV[2] AND P. A. SKOVORODKO[3]

[1]Istituto di Metodologie Inorganiche e dei Plasmi-CNR, c/o Dipartimento di Chimica Università di Bari, Via Orabona 4, Bari, 70126, Italy

[2]Laboratory of Molecular Kinetics, Institute of Thermophysics SB RAS, 1, Acad. Lavrentyev Ave., Novosibirsk, 630090, Russia

[3]Laboratory of Rarefied Gases, Institute of Thermophysics SB RAS, 1, Acad. Lavrentyev Ave., Novosibirsk, 630090, Russia

(Received 28 August 2002 and in revised form 23 September 2003)

Cold O_2/NO supersonic expansions through an axisymmetric convergent–divergent nozzle into a low-pressure background gas have been investigated both experimentally and numerically. Temperature and density measurements have been carried out, using tracer NO in an O_2 main flow. NO two-dimensional rotational temperature and density flow field patterns in the jet behind the nozzle have been measured by laser-induced fluorescence (LIF). The spectroscopic investigations are complemented by static and impact pressure measurements along the jet centreline. Two nozzles with the same inner profile but with a short and long divergent section and small and large lip have been examined. Three experiments performed using these nozzles cover a wide range of regimes of underexpanded free jet flow, from highly oscillating multi-cycle structure to the regime with smooth deceleration of the issuing flow by the background gas. The numerical simulation of the whole flow field from the conditions in the stagnation chamber to those in the flooded space is performed in the framework of the full set of Navier–Stokes equations by employing a recently developed algorithm based on a staggered grid. The flow inside a long nozzle is shown to be strongly affected by the boundary layer, which leads to the degeneration of the isentropic core at the nozzle exit and transforms the jet regime from overexpanded for inviscid flow to underexpanded for a real flow. The model reproduces the experimental structures of the low-density free jet flow fairly well.

1. Introduction

The formation of multiple expansion–compression waves in a supersonic free jet is well known, and several studies on the structure and applications of such jets are reported in the literature (Beylich 1999). In the case of a plasma jet at low power density the fluid-dynamic analysis of the expansion can be traced by optical emission (Robin, Vervish & Cheron 1994; Djakov, Enikov & Oliver 1997; De Benedictis *et al.*

† Present address: ONERA/DMPH/EAG, BP 72, 29 avenue de la Division Leclerc, 92322 Chatillon Cedex, France.

‡ Author to whom correspondence should be addressed: s.debenedictis@area.ba.cnr.it

1998; Djakov *et al.* 1999), but there are several problems that must be considered. The supersonic expansion of a molecular gas excited in a plasma chamber at relatively low pressure produces a rich flow of excited species whose energy relaxation takes place in a largely inhomogeneous fluid-dynamic environment. All the typical phenomena of an early afterglow (De Benedictis & Dilecce 1995; De Benedictis, Dilecce & Simek 1999*b*) can then contribute to the light emission from a plasma jet (De Benedictis *et al.* 1998). Moreover the coupling between the relaxation kinetics of excited species and fluid dynamics must be considered. A detailed analysis of the expansion then requires investigation of the flow field properties by appropriated diagnostics (McKenzie 1993) and by modelling.

In the framework of these basic studies we have recently examined N_2/O_2 plasma jets under various experimental conditions using laser-induced fluorescence (LIF) (Dilecce *et al.* 2000*a*; Dilecce, Vigliotti & De Benedictis 2000*b*). These investigations mainly address the atomic and molecular physics in the supersonic expansions of interest for the space shuttle re-entry into the Earth's atmosphere and for treatment of materials. In order to characterize the basics of our system we have approached an experimental–modelling study of cold-gas expansions through our nozzle configuration. The aim is to examine different fluid-dynamic descriptions (De Benedictis *et al.* 1999*b*; Broc *et al.* 2001) of the flow inside the nozzle and in the expansion chamber, which is an important step in the approach to the plasma kinetics in the jet expansion and the interaction of supersonic streams of active species with materials.

The fluid-dynamic models that have been applied to describe the flow of the type considered here can be divided into two groups: continuum and particle models. Continuum fluid-dynamic (CFD) models include those based on Euler's equations (De Benedictis *et al.* 1999*b*), the parabolized Navier–Stokes equations (Korte 1992; Skovorodko 1997) or the full set of Navier–Stokes equations (Cline 1976; Kim 1994; Gokhale & Suresh 1997). Since the applicability of the continuum description of the flow is limited to low values of the local Knudsen number (Boyd *et al.* 1992; Bird 1994; Boyd, Chen & Candler 1995) an alternative stochastic particle model based on the direct simulation of the flow at the molecular level by the Monte Carlo method (DSMC) (Bird 1994) has been applied. Besides the pure DSMC approach to the whole flow field (Campbell *et al.* 1994; Karsten *et al.* 1999), which is equivalent to the solution of the Boltzmann equation (Bird 1994), hybrid CFD–DSMC approaches have also been applied (Boyd *et al.* 1992; Boyd, Beattie & Cappelli 1994; Chung *et al.* 1995; Rosenhauer, Plähn & Hannemann 1999; George & Boyd 1999; Karsten *et al.* 1999). The choice of the appropriate fluid-dynamic model should be determined by the rarefaction degree of the flow, and the physical processes in the gas that are to be taken into account.

The experimental and numerical investigations of supersonic nozzle and plume flows available in the literature are mainly devoted to the high-vacuum background conditions that are of interest for aerospace applications (Boyd *et al.* 1992; Campbell *et al.* 1994; Rosenhauer *et al.* 1999; George & Boyd 1999). The flow inside a nozzle under conditions close to ours has been studied by Rothe (1971), whose density and rotational temperature measurements of a nitrogen flow, obtained by electron-beam fluorescence diagnostics, are often used for testing the numerical approaches (Kim 1994; Chung *et al.* 1995). Some interesting experimental and numerical results concerning the effect of finite background pressure on the plume flow of hydrogen are reported by Boyd *et al.* (1994). In spite of the available data, the main features of the free jet flow behind a supersonic nozzle with moderate pressure ratios and the

significant effect of the boundary layer inside the nozzle on jet formation have not been properly clarified.

The present experiments consider O_2/NO expansion developed from a gas reservoir at room temperature through an axisymmetric convergent–divergent nozzle into a low-pressure background gas. Temperature and density measurements have been carried out, using tracer NO in an O_2 main flow. NO two-dimensional rotational temperature and density flow field patterns in the jet behind the nozzle have been measured by LIF spectroscopy (Dilecce *et al.* 2000*a*). Under the assumption of rotational–translational equilibrium the measured NO flow field patterns represent the O_2 main flow ones. The LIF measurements are complemented by static and impact pressure measurements along the jet axis. Two nozzles with the same inner profile but with a short and long divergent section and small and large lips have been investigated. Three experiments performed using these nozzles cover a wide regime range of underexpanded free jet flow, from the highly oscillating multi-cycle structure to the regime with smooth deceleration of the issuing flow by the background gas.

A numerical simulation of the experimental flow is performed in the framework of the full set of Navier–Stokes equations, employing an algorithm based on a staggered grid that has been recently developed at the Institute of Thermophysics SB RAS, Novosibirsk. The algorithm allows the simulation of the whole flow field, from the conditions in the stagnation chamber to those in the flooded space. As the result of such an approach it is possible to treat the basic gas-dynamic phenomena determining the main features of the flow field: the flow in the vicinity of the nozzle throat determining the discharge coefficient, the flow in the divergent part of the nozzle with a significant effect of the boundary layer at the conditions considered, the change in the pattern of the flow in the vicinity of the nozzle lip due to upstream spreading of disturbances through the subsonic part of the boundary layer and, finally, the plume flow with mixing and interaction of the issuing gas with the background gas. We have not been able to find in the literature a similar approach to the simulation of the free jet flow behind a supersonic nozzle. The available simulations for viscous gas concern either the flow inside the nozzle (Cline 1976; Kim 1994; Gokhale & Suresh 1997) or the free jet flow with a prescribed distribution of the parameters in the nozzle exit section (Maté *et al.* 2001). The simulations of similar flows in the framework of a CFD–DSMC approach (Boyd *et al.* 1994; Chung *et al.* 1995), which are better suited to the regions with translational non-equilibrium effects, require much more computational resources. The analysis performed here shows that the flow field conditions of our experiments lie inside the range of applicability of the Navier–Stokes equations.

The numerical results provide a good representation of the main features of the present experimental flow, plus the distribution of some flow parameters not measured in the experiments. A discussion of the experimental limitations and of the main model assumptions provides possible reasons for some of the differences observed in the comparison between the model predictions and the experiments.

2. Experimental

2.1. *Jet apparatus and diagnostics*

The experimental apparatus is sketched in figure 1. It essentially consists of a supersonic plasma jet set-up arranged as a tower (figure 1*a*) in the laboratory surrounded by spectroscopic diagnostic apparatus with the laser set-up (figure 1*b*).

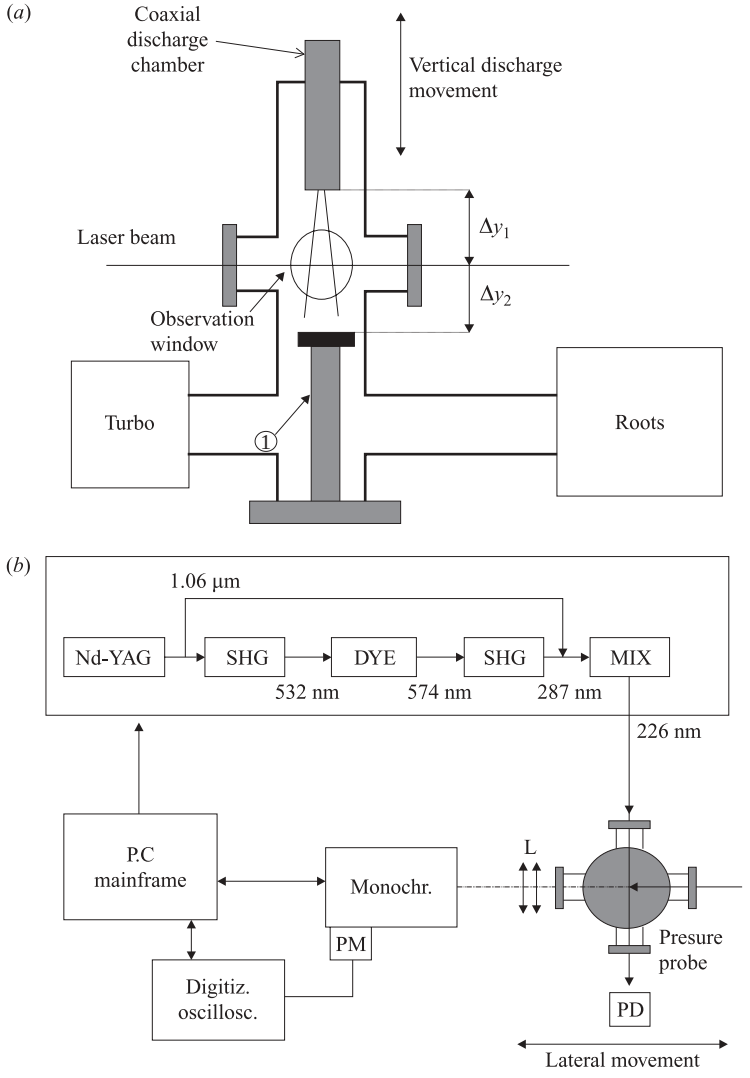

FIGURE 1. Experimental set up: (*a*) Jet expansion set-up (vertical view); (*b*) LIF laser diagnostic set-up and jet (horizontal view). 1 – Target holder.

The supersonic jet expansion is realized by passing the gas from the top of a settling chamber ($\phi = 40$ mm), through an axisymmetric convergent–divergent nozzle into a low-pressure receiver. A computer-machined stainless steel nozzle is used. The nozzle contour profile $y(z)$ is described by the following expressions:

$$y = r_* + (1/4)(z - 8m_1)^2 + (1/48)(z - 8m_1)^3/m_1, \quad 0 \leqslant z \leqslant L_c \quad \text{(convergent section)},$$
$$y = r_* + (1/3)8m_2^2 + m_2(z - 8m_1 - 4m_2), \quad L_c \leqslant z \leqslant L_c + L_d \quad \text{(divergent section)}$$

where r_* is the nozzle throat radius while m_1 and m_2 are the maximum value of the slope of the convergent section and the slope of the linear divergent section respectively. These nozzle parameters were fixed at 2 mm, 1.84 and 0.114 respectively. The divergence half-angle is 6.5°. We have examined two nozzles having the same profile and length of the convergent channel, $L_c = 14.72$ mm, but two different

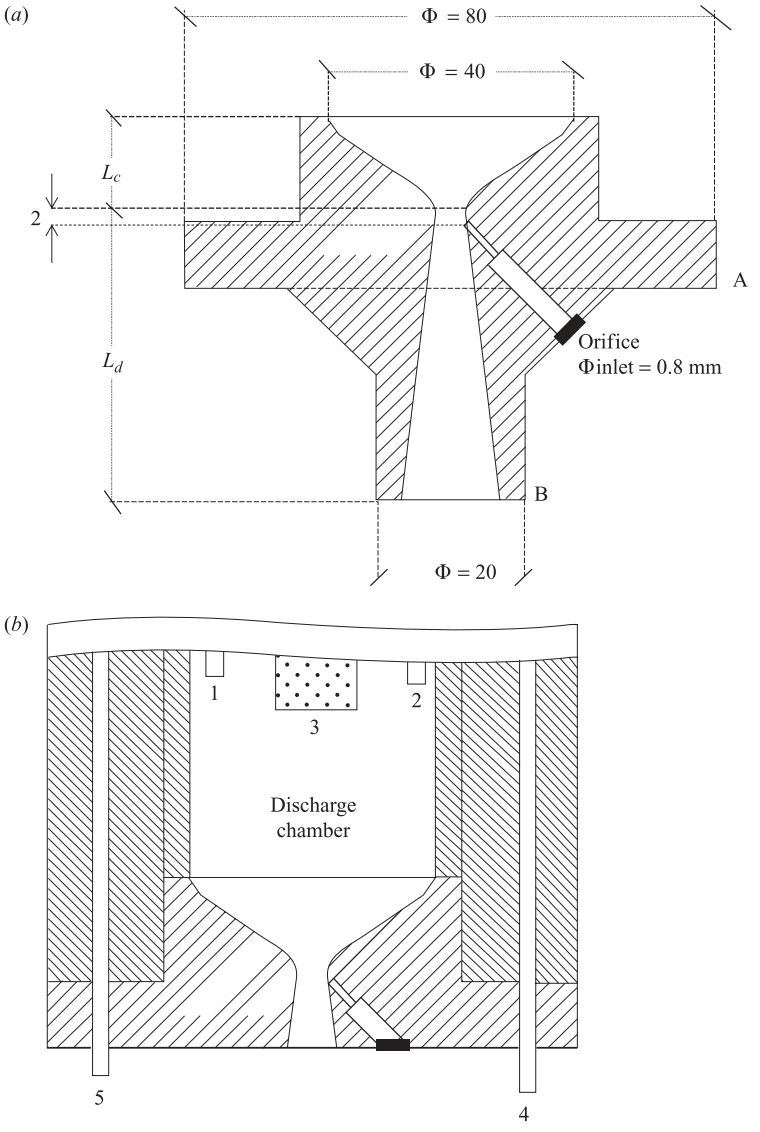

FIGURE 2. (*a*) Details of nozzle B; (*b*) assembly of nozzle A to the settling chamber (or plasma discharge chamber). 1, Gas inlet; 2, inlet pressure reading in the settling chamber; 3, electrode for RF discharge in the plasma jet configuration; 4, inlet for nozzle pressure reading; 5, tip fitting for electrical measurements.

divergent channel lengths, $L_d = 40$ mm for nozzle B and $L_d = 10$ cm for nozzle A. The latter was derived from nozzle B by shortening the divergent channel. Some details of the nozzles are shown in figure 2. The exit orifice diameter of nozzle B (shown in figure 2*a*) is 13.1 mm, and the external shape of the nozzle is characterized by a lip of 3.5 mm. The exit orifice diameter of nozzle A (also shown in figure 2*a*) is 6.3 mm and set on a flat disk whose diameter is 80 mm (the lip of the nozzle). Some probe tips are, however, still present on the surface. Figure 2(*b*) shows the assembly of nozzle A to the discharge chamber (the same for nozzle B). There was a small orifice (0.8 mm diameter), on the wall of each nozzle throat at about 2 mm in the divergent

	Exp. 1	Exp. 2	Exp. 3
L_c (mm)	15	15	15
L_d (mm)	40	40	10
O_2/NO flow rates (sccm)	900/40 ± 3	395/40 ±3	965/50 ±3
p_0 (Torr)	6.48 ± 0.04	3.24 ±0.02	6.90 ±0.04
p_b (Torr)	0.135±0.001	0.135±0.001	0.301±0.0025
T_0 (K)	300 ± 5	300 ± 5	300 ± 5
Nozzle type	B	B	A

TABLE 1. Experimental parameters: L_c, length of convergent channel; L_d, length of divergent channel; p_0, settling chamber pressure; p_b, receiver chamber pressure, T_0, stagnation temperature.

region allowing pressure measurements to be taken inside the nozzle (as sketched in the figure). In the present experiments its outlet was sealed and the fittings connecting it to the pressure meter (4 in figure 2*b*) removed in order to enlarge the optical field of view necessary for the optical measurements. Figure 2(*b*) shows the gas inlet (1) and the inlet (2) for pressure readings in the settling chamber by an external capacitance pressure meter.

The receiver chamber is pumped by a roots system. The pressure in the receiver is varied by a linear throttle-valve. The maximum settling/receiver pressure ratio is about 50 and is quite constant for a large range of flux variation (100–3000 sccm measured by a mass flow meter). In figure 1(*a*) the discharge with a jet stream impinging on the target holder is also sketched. The holder is used for putting material samples into the expansion chamber, but it has not been employed for the present experiments and its presence does not interfere with the region of the expansion that we have investigated.

The laser apparatus as well as the procedure followed for detecting NO (X) by LIF via NO γ-band excitation has been described in Dilecce *et al.* (2000*a*). The spatial resolution of LIF measurements was determined by a radiation sampling volume given by about a 2 mm laser beam cross-section and a 0.1 mm monochromator entrance slit. The radiation is sampled by 1:1 magnification optics. The settling chamber can slide axially in the expansion chamber while the whole jet apparatus can be moved on rails in the direction perpendicular to the laser beam axis and parallel to the detection axis. Both laser beam and detection axes are fixed. This arrangement allows radial space-resolved measurements of the jet at different positions along the axis. Further details can be found in Dilecce *et al.* (2000*a*, *b*).

We have investigated two expansions, one through nozzle type B ('finite' lip) and the other using nozzle type A ('infinite' lip). The details are summarized in table 1.

2.2. *Rotational temperature and density measurements*

The approach used for measuring temperature and density in the expansion region has been described in detail in Dilecce *et al.* (2000*a*), and is based on LIF measurements of rotational temperature and density of NO seeded in the main flow. Here we summarize its main aspects and assumptions. The LIF measurement of NO rotational temperature and density is carried out by the analysis of LIF spectra obtained via an excitation-detection LIF scheme based on the simultaneous excitation of two ro-vibronic transitions of the NO-γ (0,0) band from one low ($J = 2.5$) and one high ($J = 13.5$) rotational level of NO ($X\,^2\prod_{3/2}$). The fluorescence spectra are analysed by a band-fitting procedure based on the assumption of a Boltzmann distribution among

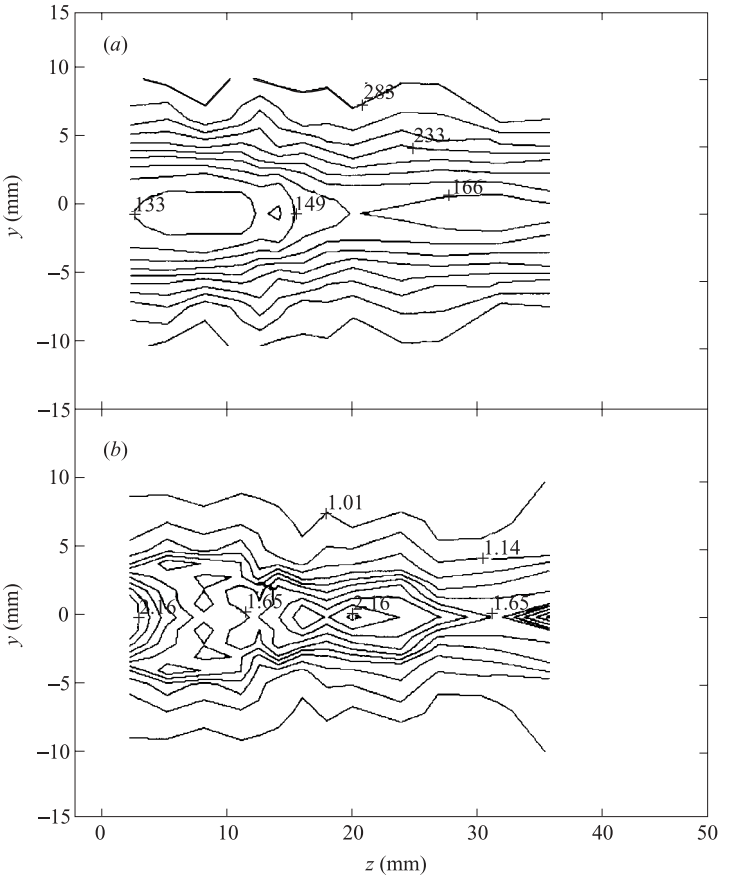

FIGURE 3. Measured contour map for Exp. 1: (*a*) NO rotational temperature, T_r; (*b*) NO background normalized density, ρ/ρ_b.

the rotational states of NO. Temperature and density measurements in the jet are calibrated on the basis of a LIF spectrum taken in a slow flowing O_2/NO reference cell at 300 K under conditions of negligible collisional relaxation. In practice we have observed that the spectra measured in the background region of the jet expansion can be used as the reference spectrum.

The NO density ρ and rotational temperature T_r values measured for (y, z) points in a jet expansion (y is the radial coordinate and z the axial coordinate referred to the nozzle exit position) are shown as two-dimensional contour plots in figures 3(*a*) and 3(*b*) for the conditions of experiment 1 (see table 1). The density values are reported as ρ/ρ_b (ρ_b is background density), while the background temperature is 300 K. Most of the conditions investigated are in the region $y \geqslant 15$ mm. The step for axial and radial measurements is not constant: finer scanning has been used in the region where flow structures were expected. Close to the nozzle the scan is limited by the presence of probe tips that interfere with the laser beam and fluorescence detection paths. The laser radial scanning was only possible in a plane almost perpendicular to that defined by the geometrical nozzle axis and the small orifice on the nozzle wall. The radial scanning was restricted to half of the section of the jet. The radial profile of the full section was measured only in a few cases to verify the symmetry of the radial profile.

2.3. *Pressure measurements*

The impact and static pressure distributions along the jet centreline were measured by different pressure probes. The end of the Pitot tube used for impact pressure measurements is a 1 mm diameter pipe tip bent at 90°, and it was inserted in the expansion chamber through a high-vacuum fitting set into the wall of the chamber facing to the optical window used for fluorescence detection. The pressure probe used for static pressure measurements, instead, ends with a tip with a closed top and the orifice is on the side of the tube 5 mm from the top. The diameter is 1 mm. The probe was aligned with the flow axis by looking for the pressure maximum during a small rotation and radial shift of the probe tip. Note that the alignment procedure used in LIF measurements is set for the geometrical axis of the nozzle, and the radial scanning recovered the signal maximum along a plane perpendicular to the laser beam only. These details are unimportant for an axisymmetric flow. The possible consequences of the alignment procedures for the results will be discussed in § 5.2.

3. Numerical algorithm

The gas flow in the nozzle and in the jet behind it were simulated by a recently developed original algorithm, based on the numerical solution of the full set of unsteady Navier–Stokes equations for axially symmetric flow of compressible perfect gas. The algorithm allows one to estimate the effect of internal energy relaxation on the flow field in the framework of a non-zero value of the bulk viscosity. The effects of velocity slip and temperature jump on the solid surfaces, which may be pronounced at the experimental conditions due to low values of the Reynolds numbers, can also be taken into account. The algorithm will be called the NS-algorithm.

3.1. *Governing equations and finite-difference scheme*

The non-conservative form of the Navier–Stokes equations for axisymmetric time-dependent flow of a perfect gas including the continuity, two momentum and the energy equations is applied in the NS-algorithm. The main points of the finite-difference scheme we have used are the following:

(i) The finite-difference approximation of the governing equations is made on a staggered grid (Harlow & Welsh 1965), where pressure, density and temperature, as well as the transport coefficients, are determined in the center of the cell, while the components of velocity are determined in the middle of the corresponding borders of the cell.

(ii) The finite-difference relations are resolved implicitly with the help of the well-known method of splitting into physical processes and spatial variables (Yanenko 1971). On each fractional step the standard tridiagonal matrix algorithm is applied.

(iii) The continuity equation is approximated according to the scheme providing conservation of variables on reaching the steady solution (or on explicit resolving of the relations).

(iv) The centred approximation of difference operators provides the second order of accuracy over spatial variables on the uniform grid.

(v) The algorithm is characterized by low implicit artificial viscosity that essentially widens the range of Reynolds numbers accessible for modelling.

The staggered grid (Harlow & Welsh 1965), is widely used for simulation of incompressible flows, but our experience indicates clear advantages of this grid for simulation of highly compressible flows too.

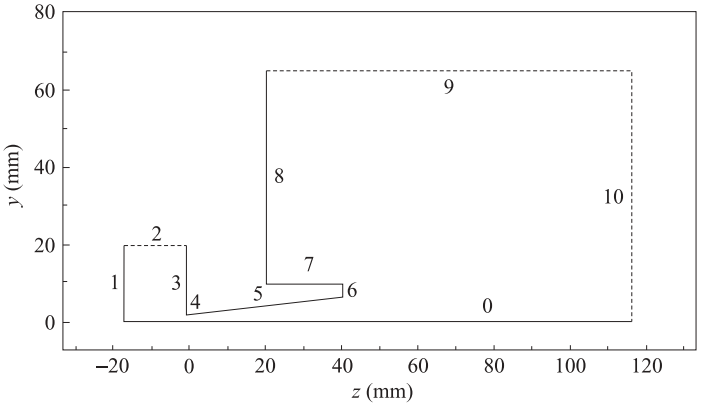

FIGURE 4. Diagram of the domain of simulation for nozzle B. The coordinates are listed in table 2 (for nozzle A see the columns z_A and y_A of table 2).

3.2. *Domain of simulation and boundary conditions*

The present version of the algorithm operates with a uniform rectangular grid with mesh sizes dy and dz in the radial and axial directions. The domain of simulation may consist of some straight-line segments parallel or perpendicular to the axis and one segment with arbitrary inclination to the axis. The cells in the vicinity of this boundary have a triangular or trapezium shape that locally modify the finite-difference relations providing the second-order accuracy of the scheme.

The algorithm does not allow the contour of the convergent part of the present nozzle to be taken into account, and it has been simplified as an orifice on a plane surface. The only attempt to treat the effect of boundary layer formation in the nozzle throat region has been made by approximating the throat region as a capillary with radius r_* and length L followed by the divergent part of the nozzle. Variation of L in the range 0 to r_* changes the flow parameters in the transonic region of the nozzle but does not modify significantly the flow in the jet region experimentally investigated. The numerical results presented below have been obtained at $L \approx r_*/2$.

Figure 4 illustrates the domain of simulation for the conditions of experiments 1 and 2 (nozzle B), which consists of 11 segments including the axis (line 0). The capillary mentioned above is shown by line 4 (0.03 mm long). Solid lines show the solid boundaries while the dashed lines correspond to permeable inlet and outlet boundaries. For the conditions of experiment 3 (nozzle A) the segment 7 is removed and lines 6 and 8 form the 'infinite' lip of the nozzle. Table 2 contains the axial and radial coordinates (in mm) of all 11 points of intersection of the adjacent segments forming the domain for both nozzles, the axial coordinates being taken from the nozzle throat (point of intersection of segments 4 and 5).

At the solid boundaries the normal component of total velocity (v_n) is prescribed to be equal to zero while the tangential component (v_t) as well as the temperature are defined by taking into account the velocity slip and temperature jump (Rae 1971):

$$v_t = -\frac{2-\alpha_v}{\alpha_v}\frac{\mu}{p}\left(\frac{\pi RT}{2}\right)^{1/2}\left(\frac{\partial v_t}{\partial n}\right)_w, \tag{3.1}$$

$$\Delta T_w = -\frac{2-\alpha_T}{\alpha_T}\frac{2\kappa}{Pr(\kappa+1)}\frac{\mu}{p}\left(\frac{\pi RT}{2}\right)^{1/2}\left(\frac{\partial T}{\partial n}\right)_w, \tag{3.2}$$

Domain segments	z_B	y_B	z_A	y_A
0–1	−17.6	0.0	−17.6	0.0
1–2	−17.6	20.0	−17.6	20.0
2–3	−0.97	20.0	−0.97	20.0
3–4	−0.97	2.0	−0.97	2.0
4–5	0.0	2.0	0.0	2.0
5–6	40.0	6.56	10.0	3.14
6–7	40.0	10.0	–	–
7–8	20.0	10.0	–	–
8–9	20.0	65.6	10.0	41.6
9–10	116.7	65.6	168.0	41.6
10–0	116.7	0.0	168.0	0.0

TABLE 2. The coordinates of the intersection points of the domain of simulation (in mm).

where n is the distance normal to the surface, p the pressure, T the temperature, μ the dynamic viscosity, κ the specific heat ratio, Pr the Prandtl number and R the gas constant. The accommodation coefficients α_v and α_T are assumed to be equal to 1 for 'slip' flow and 2 for 'no-slip' flow. There is no need to prescribe the pressure or the density at the solid boundaries.

The conditions at the inlet (segment 2) and outlet (9, 10) boundaries are defined in the same manner. The axial and radial velocities are obtained by extrapolation from internal points of the domain. The same extrapolation is applied to the density and temperature for the outlet fluxes on these boundaries. For the inlet fluxes the density and temperature are defined assuming the total enthalpy and total pressure to be the same as in the stagnation chamber for the inlet boundary and in the flooded space for the outlet boundary. Similar conditions at the inlet boundary were applied by Kim (1994). At the axis of symmetry the radial velocity as well as the radial derivatives of the axial velocity and temperature are zero.

Since the characteristic scales of the flow inside the nozzle and behind it are different, the whole geometry of the domain was divided into two partially overlapped sections for which different grid characteristics have been used. The flow in the first section, which includes the part of the domain up to the nozzle exit (segments 0 to 4, see figure 4) was calculated first with a 200×700 grid, the grid for nozzle A being the same as for nozzle B. The second section includes the part of the domain from about 2–3 mm downstream of the nozzle throat. The distribution of the parameters at the inflow boundary of this section, obtained from the flow field in the first section, was used as fixed inflow conditions. In this second section 300×600 and 200×900 grids were used for nozzle B and A respectively. The flow field for a significant part of the common region of the first and second sections proved to be the same, confirming the correctness of this approach to the whole flow field simulation.

The numerical results reported in the following have been obtained for boundary 2 being the inlet (see figure 4). It was verified that moving the inlet gas supply from this boundary to segment 1 did not modify appreciably the flow field in either the divergent part of the nozzle or in the jet.

3.3. *Transport coefficients*

The viscosity of the binary gas mixture used in the experiments was estimated in accordance with the first approximation to the exact predictions of the kinetic theory

(Hirschfelder *et al.* 1954). The temperature dependence of the dynamic viscosity of O_2 and NO components was taken for Lennard–Jones (6–12) potential with parameters $\sigma = 3.433$ Å, $\varepsilon/k = 113$ K for O_2 and $\sigma = 3.470$ Å, $\varepsilon/k = 119$ K for NO.

The Prandtl number value ($Pr = \mu C_p/\lambda$) was found to be 0.69 at $T = 300$ K for all the mixtures investigated here. The heat conductivity, λ, was estimated using the approximation recommended by Hirschfelder *et al.* (1954) for the mixture of molecular gases. The possible weak temperature dependence of the Prandtl number on the flow field was estimated and found to be insignificant.

The bulk viscosity μ' is expressed by the relation (Hirschfelder *et al.* 1954)

$$\mu' = pRC_r\tau_r/C_v^2, \tag{3.3}$$

where C_r is the heat capacity of the internal energy, C_v the total heat capacity at constant volume, and τ_r is the rotational relaxation time. The bulk viscosity in the present conditions is mainly determined by the rotational relaxation of O_2. The available data for rotational collision number Z for O_2–O_2 collisions at room temperature are characterized by a large scatter in the range $Z = 2$–20 (O'Neil & Brokaw 1963; Lambert 1977). Therefore for our purposes we take the compromise value $Z = 5$, which leads to the value of $\mu' = 0.6\mu$, taking into account the known relation for the mean time, $\tau_t = \pi\mu/4p$, between collisions of molecules.

3.4. *Determining the parameters*

For the numerical solution the variables ρ, p, T, and radial (u) and axial (w) components of total velocity $\boldsymbol{v}$ were normalized to the corresponding parameters in the stagnation chamber, including the sound speed c_0. The stagnation temperature T_0, the nozzle wall temperature T_w and the temperature T_b of the gas in the undisturbed background region of the receiver chamber were assumed to be 300 K.

The Reynolds number, $Re_0 = \rho_0 c_0 r_*/\mu_0$ is equal to 355.9, 178.2 and 379.0 for experiments 1, 2 and 3 respectively. At these low Reynolds numbers a strong influence of the boundary layer on the flow inside the nozzle is to be expected (Rothe 1971). The effects of velocity slip and temperature jump should also be analysed due to their possible influence on the flow.

The value of $\kappa = 7/5$ has been used for a binary mixture of diatomic gases in the temperature range $T < 300$ K.

The calculations were made for two values of the bulk viscosity: $\mu' = 0$ and $\mu' = 0.6\mu$. Also, for each value of μ' the variants with and without slip effects were calculated. We will illustrate in detail the results obtained for the basic variant $\mu' = 0.6\mu$, $\alpha_v = \alpha_T = 1$. Some important results for other variants will also be discussed. Attention will be focused on results that can be compared with experimental data or are useful for their interpretation.

3.5. *Discharge coefficients*

The discharge coefficient g represents the ratio of gas flow rate to the corresponding value for one-dimensional isentropic flow. As a rule, for real flows $g < 1$, depending on factors due to the viscous or inviscid nature of the flow. These factors are difficult to separate in a real flow but it is possible to estimate them numerically. The purely viscous contribution to the decrease of g can be obtained using the so-called 'slender-channel' approximation (Rae 1971) assuming the pressure to be constant in the radial direction.

Table 3 shows the g values calculated from experimental data and by the numerical models with and without taking into account slip effects. The 'SC' values correspond

	SC, Slip	SC, No-slip	NS, Slip	NS, No-slip	Experiment
Exp. 1	0.889	0.875	0.829	0.815	0.839 ± 0.017
Exp. 2	0.844	0.818	0.791	0.776	0.775 ± 0.016
Exp. 3	0.892	0.878	0.832	0.818	0.851 ± 0.017

TABLE 3. Flow rate discharge coefficients. SC denotes the slender channel approximation and NS the predictions of the Navier–Stokes algorithm.

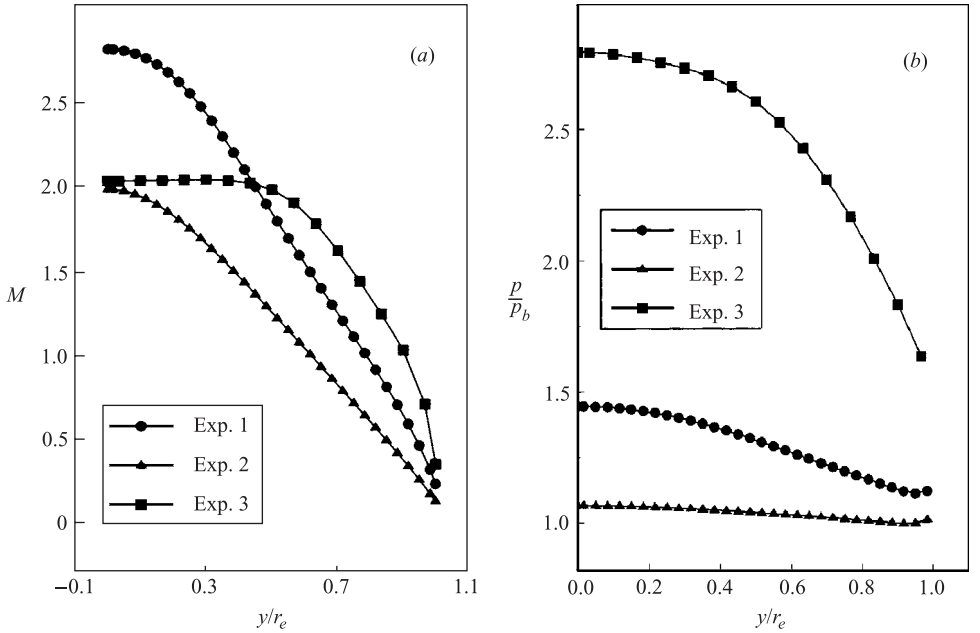

FIGURE 5. Calculated radial profiles of (*a*) Mach number and (*b*) background normalized pressure, in the nozzle exit section for experiments 1, 2 and 3.

to the 'slender-channel' approximation for the exact contour of the nozzle, while 'NS' values are the predictions of the NS-algorithm. The SC-approach predicts, as expected, higher g values than the NS-approach. The g values increase when taking into account slip effects, but differences between 'slip' and 'no-slip' values are practically the same in both approaches. SC-values overestimate by about (3–8)% the experimental g values, while the NS-values range (from −2.0% to +3.9%) around them. Taking into account that the accuracy of the experimental g values is about ±2% (propagation error due to pressure, flow rate and stagnation temperature uncertainties) we conclude that the best agreement with experiment is achieved, as expected, for the 'NS, slip' variant.

3.6. *Nozzle exit parameter*

An important characteristic of the flow, that determines the structure of the underexpanded free jet behind the supersonic nozzle, is the distribution of parameters in the nozzle exit section. Figure 5(*a*) shows the radial profiles for the Mach number ($M = ((u^2 + w^2)/\kappa RT)^{1/2}$) and figure 5(*b*) the pressure, calculated for the three experiments. The radial coordinate y is normalized to the nozzle exit-orifice radius r_e, and the pressure to the background pressure p_b. The points shown exhibit

the computational grid used. The pressure is not defined on the solid surface since it coincides with the border of the cell of the grid (see § 3.1(i)).

The Mach number profiles for the long nozzle B (Exp. 1 and Exp. 2), being quite similar and without any indication of an isentropic core, differ significantly from that for the short nozzle A (Exp. 3), where the pronounced isentropic core occupies about half of the profile. In the vicinity of the nozzle wall considerable velocity slip ($M \sim 0.15$–0.36) is observed due to acceleration of the flow caused by the streamwise pressure gradient. A similar result is seen from the pressure profiles. In the vicinity of the wall a significant negative pressure gradient is observed for Exp. 3, in contrast with Exp. 1 and Exp. 2 with almost constant pressure there.

The nozzle exit Mach number for one-dimensional isentropic flow is equal to 4.004 for the long nozzle (B) and 2.427 for the short nozzle (A). The corresponding values of the pressure ratio p/p_b are equal to 0.314 for Exp. 1, 0.157 for Exp. 2 and 1.46 for Exp. 3. The comparison between these data and those presented in figure 5 demonstrates a strong effect of the boundary layer on the nozzle exit parameters at the conditions considered – for inviscid flow, the jet even becomes overexpanded for Exps. 1 and 2 and slightly underexpanded for Exp. 3. For viscous flow the distribution of parameters at the nozzle exit depends on the background pressure due to upstream spreading of disturbances through the subsonic part of the boundary layer. In the range of parameters examined, no separation effect is observed inside the nozzle.

Regarding the supersonic character of the flow in the near-axis region and the mean value of the pressure ratio (p/p_b), one should expect a multi-cycle structure of the jet flow in Exp. 3, a smooth deceleration of the issuing flow in the near-isobaric conditions in Exp. 2 for which the exit pressure is close to the background one, and a jet flow with character intermediate between those for Exp. 2 and Exp. 3 in the case of Exp. 1.

3.7. *Test computations*

Numerous computations were performed to test the confidence in the solution obtained from the finite-difference scheme as the solution of the initial differential equations. Besides tests of the internal nature (varying the size of the domain of simulations, the parameters of the grid, the effect of the boundary conditions, etc.) further computations were performed for supersonic nozzle and plume flows of various experiments found in the literature. As an example, the results for the conditions of Rothe's (1971) experiments, obtained for the no-slip boundary case, were found to be in good agreement with similar numerical results reported by Kim (1994). Taking account of the effects of velocity slip and temperature jump improves the agreement between the measured data and those calculated for no-slip flow. The main conclusion of these tests is that the algorithm should give a good description of two-dimensional compressible flow provided the flow conditions are in the range of applicability of the Navier–Stokes equations.

4. Results and comparison with the fluid-dynamic model

4.1. *Experiment 1*

The most complete set of measurements was carried out for this experimental condition. The contour maps of the rotational temperature and density of NO in figures 3(*a*) and 3(*b*) clearly show the presence of two expansion–compression waves at about 10 mm and 35 mm from the nozzle exit.

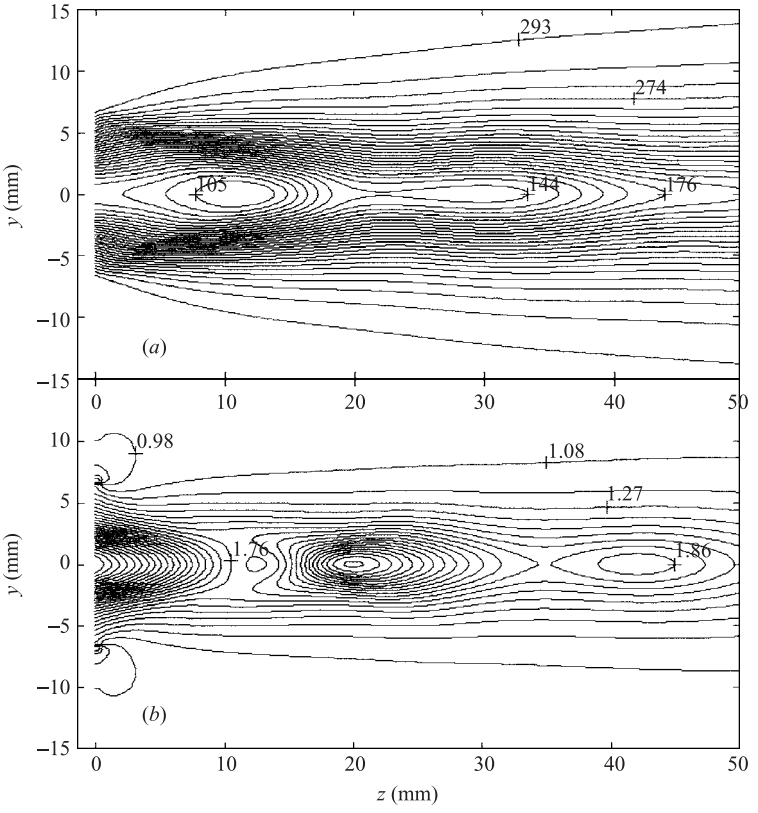

FIGURE 6. Calculated contour map for Exp. 1: (*a*) gas temperature T; (*b*) background normalized density, ρ/ρ_b.

The contour maps calculated for the same experimental conditions by the fluid-dynamic model in its basic variant (see § 3.4) are reported in figures 6(*a*) and 6(*b*). No Mach disk configuration seems to appear in the space region examined. An intercepting shock with a regular reflection is clearly seen at about 10 mm from the nozzle exit. Despite the noisy character of the experimental maps in figure 3 the qualitative structures of the expansion and their positions are well reproduced.

The measured and calculated axial profiles are reported in figures 7(*a*) for temperature and 7(*b*) for density (here and below the numerical results designated as Mod. (1) correspond to the basic variant, while Mod. (2) designates the results with 'no-slip' boundary conditions on solid surfaces; the results designated as Mod. (3) were obtained for the basic variant in the plane parallel to the axis but shifted from it by 1.5 mm will be discussed in § 5.2. As can be seen from figure 7, both measured and calculated profiles reveal a periodic (spatially oscillating) jet structure and are in good qualitative agreement though there are noticeable differences between them. The calculated temperature underestimates the measured one – along the axis the difference of about 25 K is attenuated at longer distance. The density, on the contrary, is overestimated and significant deviations occur in the region close to the maxima. The calculated position of the temperature and density minima is slightly shifted towards larger z values. The calculations show four damped oscillations in the z region 0–80 mm.

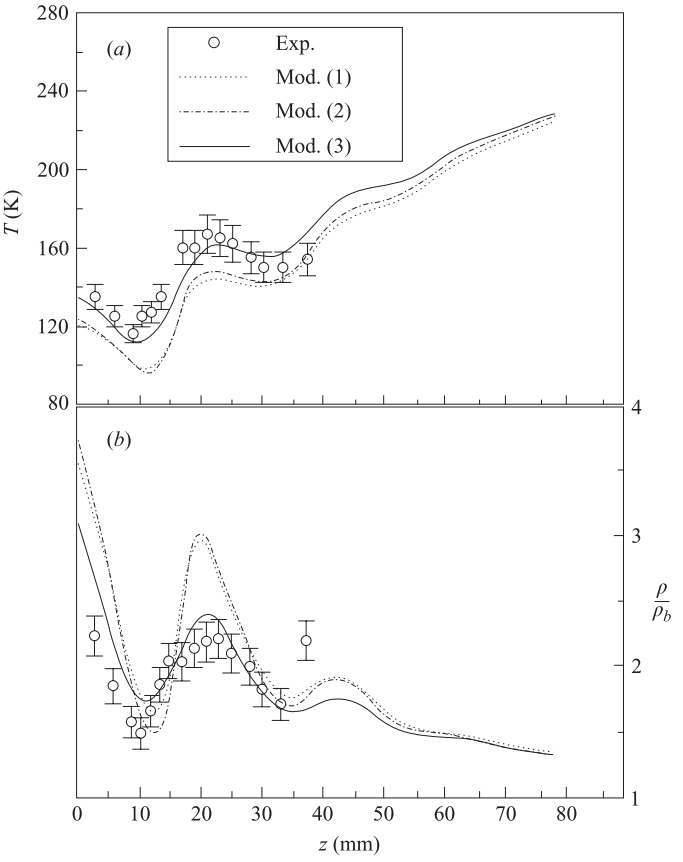

FIGURE 7. Comparison of (*a*) temperature and (*b*) density axial profiles measured and calculated under conditions of Exp. 1. Mod. (1) and Mod. (2) are models with and without slip effects respectively. Mod. (3) is model with a lateral shift in the axis of 1.5 mm.

Figure 8 reports the radial profiles of temperature and density for two distances from the nozzle exit close to the compression wave position. For both distances the difference between the experimental and calculated profiles in the region near the axis is significant.

The structures of the jet are confirmed by the static and impact pressure measurements at the centreline of the jet. The measured and calculated pressure axial profiles are shown in figure 9. In accordance with the criterion reported by Boyd *et al.* (1992) no correction for rarefaction effects was made to the ideal values of the Pitot pressure (total pressure behind a straight shock, p_0') calculated from the numerical flow field. While the impact pressure (figure 9*b*) is reproduced well by the calculation, the measured static pressure (figure 9*a*) shows lower amplitude oscillations. The positions of the measured oscillations are slightly ahead of those calculated, confirming the differences noted in the axial density case.

We recall that for the impact pressure the position of the probe on the centreline was checked by a small rotation and radial shift of the tip. In the background region the pressure reading was found to be independent of the rotation of the tip. The static pressure, on the other hand, is very sensitive to the design of the probe tip and the position of the side orifice. We have tested several probes having different thickness

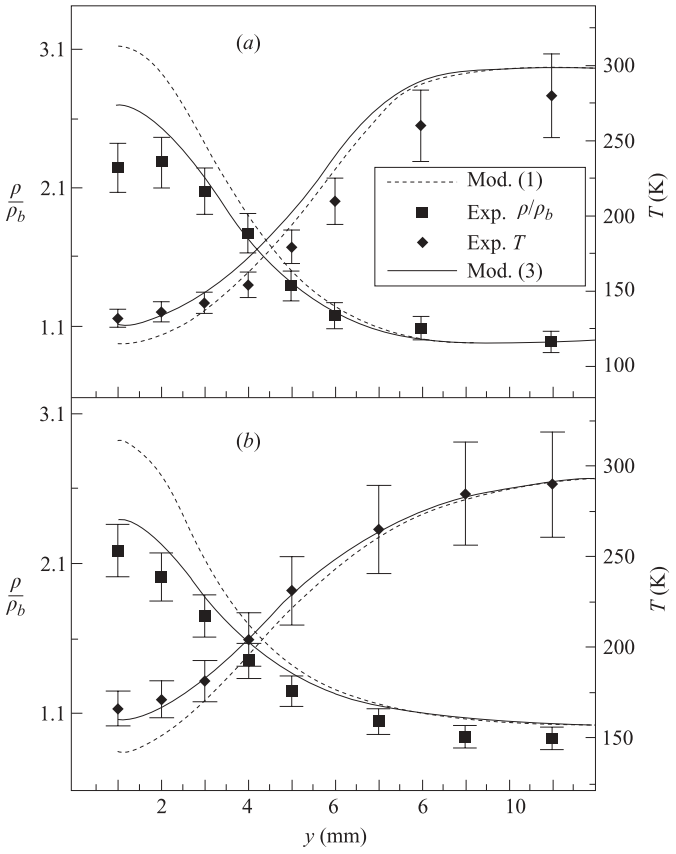

FIGURE 8. Comparison of calculated and measured radial profiles of temperature and density at distances from the nozzle exit (*a*) $z = 3$ mm and (*b*) $z = 21$ mm for Exp. 1. Models with slip effects (1) and lateral shift in the axis of 1.5 mm (3). Mod (1) and (3) defined in figure 7.

of the tip and position and diameter of the orifice. But, as shown in figure 9(*a*) we obtained different readings even though the patterns remain qualitatively the same. The difference shown in figure 9(*a*), for two different probe designs, therefore, can be taken as the uncertainty in these trends.

The reasons why the flow is described better by the axial impact and static pressure distributions than by LIF measurements will be examined in § 5.2.

4.2. *Experiment 2*

In this experiment the stagnation pressure was halved while maintaining the same pressure in the receiver chamber. The measured and calculated axial profiles of temperature and density in figures 10(*a*) and 10(*b*) show weak structures over increasing and decreasing temperature and density trends respectively. Underestimation of the temperature and overestimation of the density by the calculations confirm the remarks made for Exp. 1. Despite these differences, the values of normalized static pressure inferred from the measured temperature and density ($p/p_b = (\rho/\rho_b)(T/T_b)$) values are close to unity, in agreement with the model prediction and the nearly isobaric character of the jet flow under the conditions of Exp. 2 (see the discussion of figure 5).

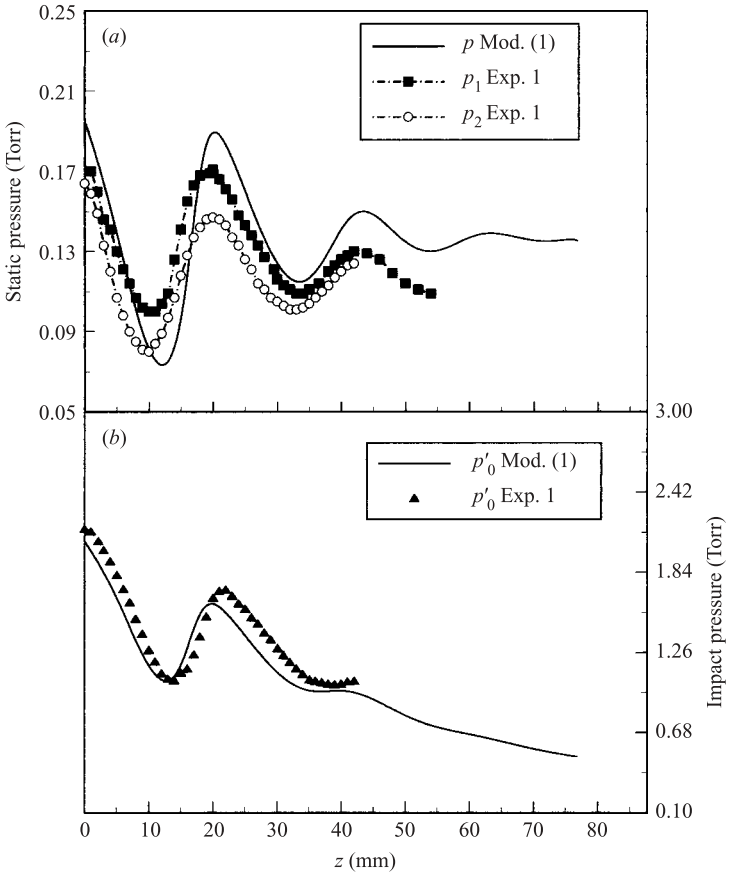

FIGURE 9. Comparison of axial profiles of (*a*) static and (*b*) impact pressure measured and calculated under conditions of Exp. 1. Mod. (1), model with slip effects. Measurements of static pressure taken with two probe designs. Mod (1) as in figure 7.

4.3. *Experiment 3*

In this experiment, the divergent channel of the nozzle used for Exp. 1 and Exp. 2 has been cut, giving an exit orifice diameter and a divergent channel length lower than in Exp. 1. The measured and calculated axial temperature and density trends are shown in figures 11(*a*) and 11(*b*). This fluid-dynamic flow condition is rich with structures due to the supersonic character of the flow and sufficiently high values of the pressure ratio (p/p_b) at the nozzle exit that predetermines the multi-cycle structure of the jet flow (see the discussion of figure 5). In the experiment three main expansion–compression waves can be clearly identified. The three weak waves that follow are submerged within the scatter of the experimental data and can be seen in the calculations only. The agreement is qualitatively good, although differences are still present.

5. Discussion

To understand the differences observed between measured and calculated temperature and density flow fields, some aspects of the measurements and of the model need to be discussed.

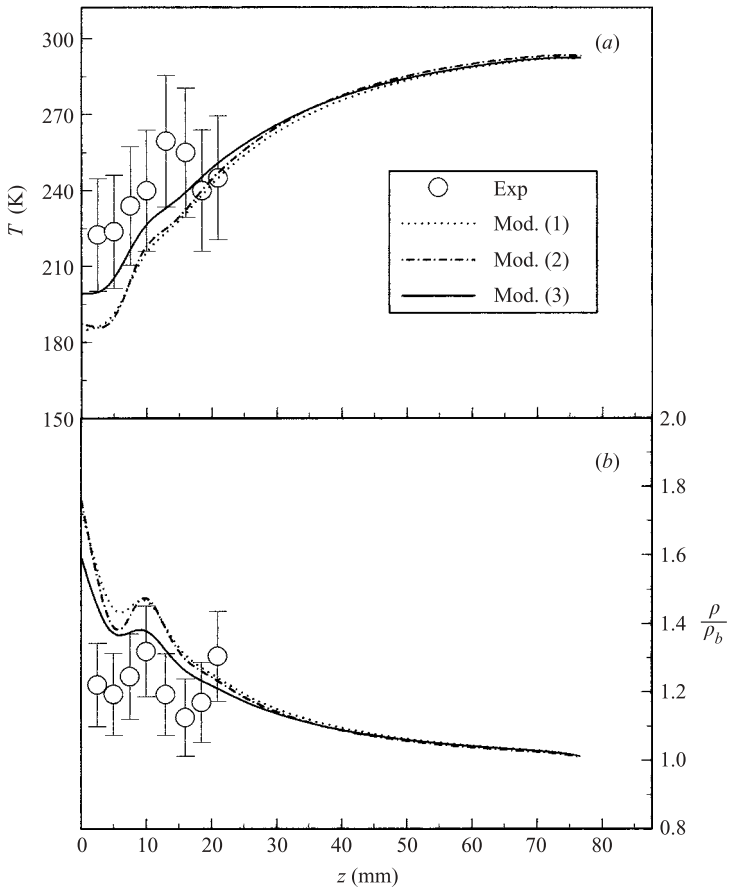

FIGURE 10. Comparison of (*a*) temperature and (*b*) density axial profiles measured and calculated under conditions of Exp. 2. Models with (1) and without (2) slip effects. Model with lateral shift in the axis of 1.5 mm (3). Mods. (1)–(3) as in figure 7.

5.1. *The experiments*

A detailed discussion on the accuracy of the measurements is given by Dilecce *et al.* (2000*a*). Here we summarize the main points.

(i) *Statistical error*. This is due to the accuracy of the intensity measurements for the LIF spectrum of the sample and of the reference cell, taking into account the error propagation of the laser intensity fluctuations. This is shown as error bars on the experimental points shown in the figures. Exp. 1 was carried out with a larger number of samplings per point, thus with a lower statistical error than in Exps. 2 and 3.

(ii) *Long-time-scale drift of the dye laser wavelength and/or bandwidth*. This drift is essentially thermal. It produces a difference between spectra taken at different times. It has been minimized.

(iii) *NO translational–rotational equilibrium*. Assuming this equilibrium, the measured T_r (NO) can be compared to the gas temperature calculated by the model. This assumption is probably not fully satisfied under the rarefied conditions achieved in the expansion phase of the gas. The effect of R–T relaxation on the difference

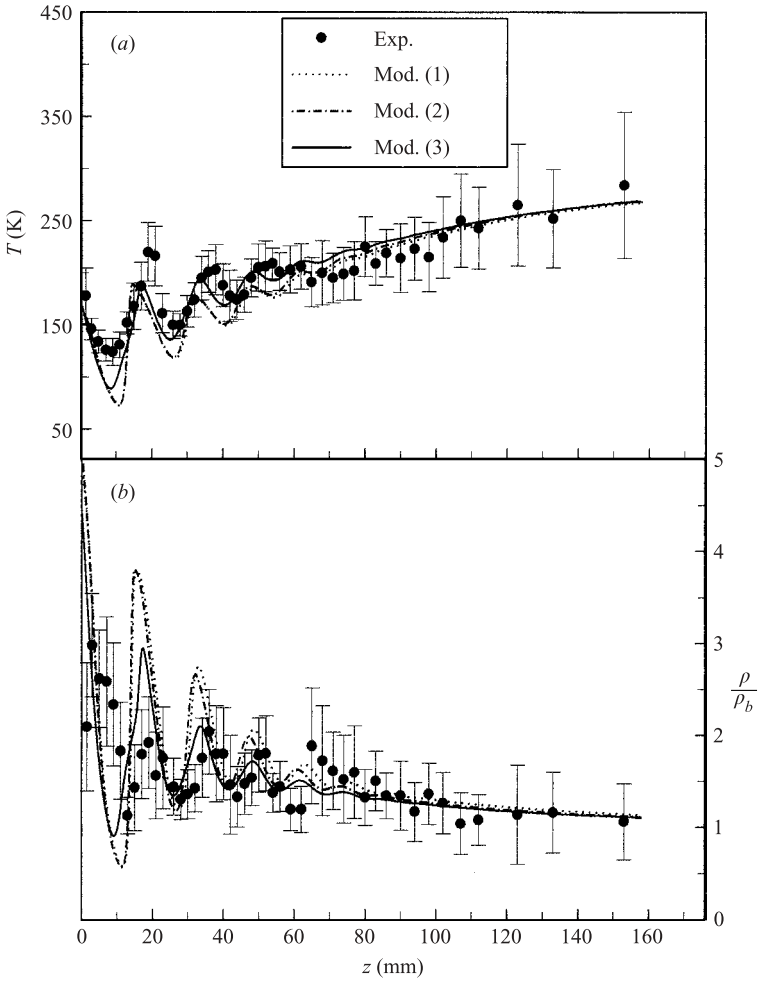

FIGURE 11. Comparison of (*a*) temperature and (*b*) density axial profiles measured and calculated under conditions of Exp. 3. Models with (1) and without (2) slip effects. Model with lateral shift in the axis of 1.5 mm (3). Mods. (1)–(3) as in figure 7.

between the measured T_r (NO) and T calculated by the model will be discussed in the following section.

(iv) *Cluster formation and/or condensation of NO*. In the experiments by Brechignac *et al.* (1985, see also references therein), NO dimers were produced in a molecular beam and in a cell under suitable pressure/temperature conditions. At our pressure/temperature condition cluster formation is probably not significant since NO is a minor specie in the mixture. From analysis of the experimental data reported by Golomb & Good (1968), to obtain a 1% concentration of NO dimers in the flow field the stagnation pressure should be larger at least by one order of magnitude than that in our cases.

(v) *Spatial averaging due to finite laser beam cross-section.* An upper limit of this effect on the computed flow field was estimated by assuming a homogeneous laser beam exciting a cylindrical volume of 2 mm diameter and 2 mm in length. The calculated averaged flow field data over a cylinder show a smoothing of axial

distributions of temperature and density, but the smoothing effect amounts to about 15% while the observed disagreement between theory and experiment is about 55% (see figure 7).

5.2. *The model*

We have considered the following points:

(i) *Effect of species separation in the flow field.* This effect was evaluated with a different algorithm based on the parabolized Navier–Stokes equations (Skovorodko 1997), adopted for treating the effect of non-zero pressure in the flooded space. The algorithm allows the effects of concentration, pressure and thermal diffusion to be taken into account. It was found that: (*a*) the effect of thermal diffusion at the experimental conditions is negligible; (*b*) the effect of pressure and concentration diffusion may change the NO concentration in the jet by less than 1%, 0.2% and 4% for experiments 1, 2 and 3, respectively. The small O_2 and NO mass difference leads to a weak pressure-diffusion effect.

(ii) *Rotational relaxation.* A complete analysis of the NO rotational relaxation in the NO/O_2 system cannot be carried out because of the lack of the necessary basic data (Holmes, Jones & Lawrence 1964; Bauer & Sahm 1965; Lambert 1977). However, the extent of the rotational non-equilibrium effects on the flow field has been demonstrated by simulations made for two values of bulk viscosity ($\mu' = 0$ and $\mu' = 0.6\mu$). We have considered that, for $\mu' \neq 0$, the temperature T entering the governing equations should be treated as the mean of the rotational T_r and translational T_t temperatures according to the diatomic gas relation:

$$2.5T = 1.5T_t + T_r. \tag{5.1}$$

Furthermore, from the definition of the bulk viscosity (Hirschfelder *et al.* 1954), T_t and T are related by

$$\rho R T_t = \rho R T - \mu' \mathrm{div}\, \boldsymbol{v}, \tag{5.2}$$

Then, temperatures T_r and T are related by

$$\rho R T_r = \rho R T + 1.5\mu' \mathrm{div}\, \boldsymbol{v}. \tag{5.3}$$

From the above relations it is found that the difference between the temperatures, $\Delta T = T_r - T$, will have different signs in the expansion and compression regions of the flow. In our conditions the absolute value of ΔT does not exceed 10 K, thus confirming the applicability of the concept of bulk viscosity approach, while the difference in the values of density for $\mu' = 0$ and $\mu' = 0.6\mu$ does not exceed few percent. This excludes the possibility that the systematic underestimation of the temperature and overestimation of the density axial profiles in our comparisons is due to the rotational relaxation.

(iii) *Non-exact contour of the convergent part of the nozzle in the model.* The experimental investigations concerning the effect of the subsonic part of the nozzle contour on the flow field of the free jet behind the sonic nozzle (Ashkenas & Sherman 1966; Murphy & Miller 1984) indicate that this effect is significant only close to the nozzle throat (within about few nozzle diameters) where large gradients of the jet parameters are present. This effect should be considerably reduced in our supersonic nozzles in view of the lower values of the Reynolds numbers and the moderate half-angle of the nozzle expansion (6.5°). The small effect of the capillary in the nozzle throat region on the flow field (§ 3.2) gives a further indication that our approximation is not significantly different from the real flow in the nozzle and in the plume. A high

conservation of the flow field with respect to the parameter profiles in the nozzle throat is also reported by Boyd *et al.* (1994) for flows similar to ours.

(iv) *Effect of the nozzle wall temperature.* The estimations indicate that in our experiments the difference between the nozzle wall temperature and the stagnation temperature is small. Nevertheless we checked the possible effect of the nozzle wall temperature on the flow field, taking into account the strong effect of the boundary layer. The simulations for an adiabatic wall reveal that the change of parameters affects the flow inside the nozzle significantly more than in the plume. This is due to the opposite effects produced by the pressure and the Mach number in the nozzle exit section on the jet flow field. The extent of density and temperature changes in the plume calculated for two limiting T_w values was not significant compared to the differences between theory and experiment.

(v) *Effect of velocity slip and temperature jump.* The axial distributions of temperature and density calculated for 'slip' (Mod. (1)) and 'no-slip' (Mod. (2)) flows, shown in figures 7, 10 and 11, are quite similar for all three experiments despite the noticeable value of the slip velocity at the nozzle exit (see figure 5). Slip effects appear insignificant because the opposite effect of the other parameters in the nozzle exit section compensates the changes in the plume flow field as mentioned above. Possible uncertainties in the values of accommodation coefficients, or the approximate nature of the slip theory do not affect the insignificance of the slip velocity and temperature jump in the present conditions.

(vi) *Limited applicability of the Navier–Stokes equations.* It is well known that the Navier–Stokes equations cannot adequately describe the gas flow in a region several mean free paths thick near the surface (the Knudsen layer) as well as in front of a strong shock wave (Bird 1994). Both these fluid-dynamic elements are present in the flows of our concern. We searched for the regions of the flow where the applicability of the continuum approach is questionable by applying the procedure proposed by Boyd *et al.* (1995), based on the gradient-length local (GLL) Knudsen number:

$$(Kn)_{GLL} = \frac{l}{Q}\left|\frac{\mathrm{d}Q}{\mathrm{d}s}\right|, \tag{5.4}$$

where l is the local mean free path, Q is the flow property (density or temperature), and s is some distance between two points in the flow field. The applicability condition is

$$(Kn)_{GLL-D} < 0.05, \tag{5.5}$$

where $(Kn)_{GLL-D}$ is the Knudsen number based on the density ($Q \equiv \rho$).

The results of this analysis may be summarized as follows: (*a*) the region inside the nozzle lies within the region of applicability of the Navier–Stokes equations for all experimental regimes; (*b*) for the near-axis region of the jet, flow condition (5.5) is fulfilled for Exp. 1 and Exp. 2, but for Exp. 3 there is a narrow region in the first shock front at $z \sim 13$ mm (see figure 11*b*) where the GLL Knudsen number reaches the value 0.074; (*c*) for all the regimes there is a region in the vicinity of the beginning of the nozzle lip (segment 6 in figure 4) where condition (5.5) is not fulfilled due to large density gradients. The size of this region is $\delta z = 1.5$ mm, $\delta y = 2.2$ mm for Exp. 1, $\delta z = 0.7$ mm, $\delta y = 1.1$ mm for Exp. 2 and $\delta z = 1.5$ mm, $\delta y = 1.3$ mm for Exp. 3. The relatively small size of the zone where the continuum description of the flow is not adequate would not lead to significant disturbances of the main flow field.

Besides the present estimations, a direct simulation of the flow field for Exp. 1 was performed in the framework of the CFD–DSMC approach, which is similar to

that used by Chung *et al.* (1995). The calculations, not reported here, confirm the Navier–Stokes model predictions and the difference with the experimental results. This test indicates clearly that the disagreements we found do not arise from the approximate nature of the model.

(vii) *Non-axial symmetry of the flow*. The characteristic of axisymmetric flows is the focusing of the disturbances on the axis where the maximum amplitude of oscillations occurs. Any deviation from the axis leads to the decrease of this amplitude (see figures 3, 6, and 12 below). The presence of the orifice in the nozzle throat region may cause a perturbation of flow axisymmetry. However, the LIF radial scanning cannot detect such a shift, since it is made in a direction almost perpendicular to the geometrical nozzle axis–orifice plane. Therefore the effect of the orifice disturbances was experimentally investigated in 2002 in a side experiment by S. Ya. Khmel & E. A. Baranov (personal communication) in a free jet of nitrogen ($p_0 = 6.5$ Torr, $T_0 = 297$ K), expanding into vacuum through a nozzle with the same profile as our nozzle B, with an orifice (0.8 mm in diameter) in the nozzle wall in the throat region. Before the experiment the orifice was sealed on the external surface of the nozzle. Using the electron beam fluorescence diagnostics (Rebrov *et al.* 1981) the radial profile of the density in the jet was measured 30 mm from the nozzle exit, in the plane defined by the orifice and the geometrical axis. The position of the maximum of the radial profile was found to be shifted in the direction opposite to the location of the orifice by about 1 mm with respect to the nozzle geometrical axis, while no shift was observed for the same flow before creating the orifice. This confirms that the interpretation of our model–experiment comparison is affected by the orifice perturbation. We have searched numerically for the amount of lateral shift of the flow axis necessary to improve the comparisons in figures 7, 8, 10 and 11, assuming that the main structure of the flow remains similar to the axisymmetric one for some new position of the 'axis'. The results obtained for a lateral shift of the axis of 1.5 mm reported in the same figures (Mod. (3)) demonstrate a substantial improvement. This interpretation can also explain why the model agreement is better with pressure probe measurements than with LIF measurements. The pressure probe alignment procedure allows it to be set as close to the true position of the flow axis as possible. We conclude that the observed differences between theory and experiment are mainly connected with the disturbances of the flow field caused by the orifice in the nozzle wall in the throat region.

5.3. *Flow characteristics*

The present numerical model can be used to predict details of the distribution of flow parameters not measured in the present experiments.

Figure 12 shows the streamlines of the flow behind the nozzle for the conditions of Exp. 3. The flow rate values are normalized to the ideal value of the gas flow rate through the nozzle. The picture gives a good representation of the process of mixing of the gas issuing from the nozzle with the background gas. In the periphery of the flow the background gas moves in a direction almost normal to the axis, which reflects the 'suction' ability of the jet, used in jet vacuum pumps (Beylich 1999). Damping oscillations of streamlines are observed in the near-axis region; this reflects the multi-cycle structure of the flow typical of overexpanded and slightly under-expanded free jets.

Figure 13 shows the Mach number axial profiles calculated for the present experiments. The first shock is formed outside the nozzle channel where the first

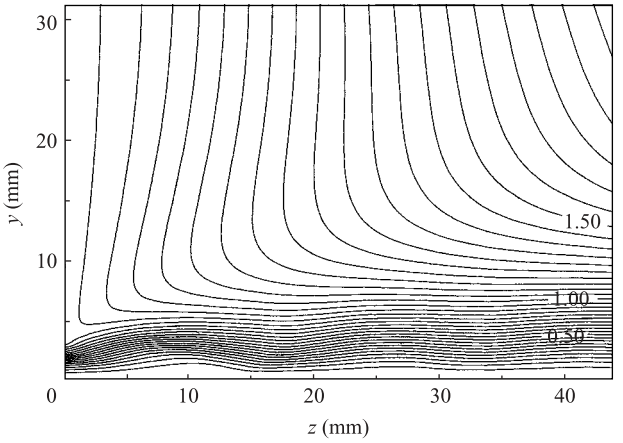

FIGURE 12. Streamline picture of the flow behind the nozzle under conditions of Exp. #3.

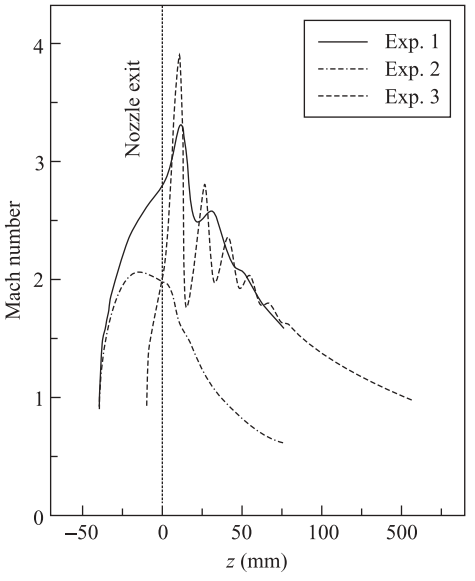

FIGURE 13. Calculated axial profiles of Mach number for Exps. 1, 2 and 3. (Note that the profiles start from the nozzle throat position.)

Mach number maximum occurs. The flow behind the shock remains supersonic, i.e. the shock is oblique and no Mach disk is formed in the plume. Such regular reflection of the shock from the axis typically occurs in the free jet of a supersonic nozzle at moderate pressure ratios (Boyd *et al.* 1994; Chung *et al.* 1995).

In Exp. 2 the Mach number reaches the maximum value inside the divergent part of the nozzle but this maximum does not indicate shock formation since the density decreases monotonically. Such a behaviour of the Mach number is connected with the spreading of the boundary layer region up to the flow axis and the degeneration of the isentropic core due to the low value of the Reynolds number. Similar features of the flow inside the nozzle at low Reynolds numbers were observed by Rothe (1971).

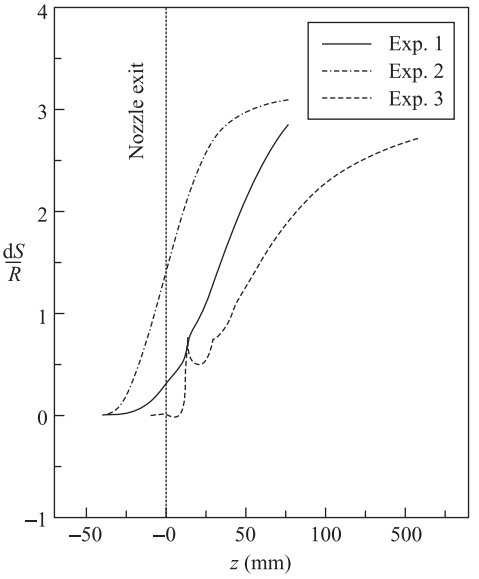

FIGURE 14. Calculated axial profiles of entropy increment $\mathrm{d}S/R$ for Exps. 1, 2 and 3.

This view is confirmed by the results in figure 14, showing the axial distributions of the entropy increment $\mathrm{d}S/R$

$$\frac{\mathrm{d}S}{R} = \frac{1}{(\kappa - 1)} \ln \frac{T}{T_0} - \ln \frac{\rho}{\rho_0},$$

for our experiments. The isentropic flow corresponds to the condition $\mathrm{d}S/R = 0$. The axial dependence of $\mathrm{d}S/R$ is qualitatively the same for all the cases but for Exp. 2 a sharp increase of $\mathrm{d}S/R$ takes place inside the nozzle. It should be noted that the local maximum of $\mathrm{d}S/R$ inside the region of the first shock wave for Exp. 3 is a known characteristic of the shock wave structure connected with the existence of a local maximum of entropy increment in the shock front (Zel'dovich & Raizer 1967).

6. Concluding remarks

Laser-induced fluorescence applied to NO gas seeded in an O_2 main flow allows tracing the main flow field properties (temperature and density) of the gas expansion through a de Laval nozzle into a low-pressure background gas. Three experiments performed on two different supersonic nozzles cover a wide range of regimes of underexpanded free jet flow, from highly oscillating multi-cycle structure to a regime with smooth deceleration of the issuing flow by the background gas. An essential feature of the flow for the long nozzle (B) is the strong effect of the boundary layer on the flow inside the nozzle, which leads to the degeneration of the isentropic core at the nozzle exit and transforms the jet regime from overexpanded for inviscid flow, to underexpanded for a real flow.

The agreement between Navier–Stokes model predictions and experimental data is qualitatively satisfactory. The structure of temperature and density fields observed in the plume is reproduced well by this fluid-dynamic description. Differences are observed in the values of the temperature and density in the regions of compression

waves. Such differences must be ascribed mainly to the non-axial symmetry of the flow due to the presence of the orifice in the nozzle wall. The unexpectedly high sensitivity of the plume flow to disturbances at the supersonic nozzle wall in the throat region at low Reynolds numbers should be taken into account on planning similar experiments.

The algorithm for numerical solution of the full set of Navier–Stokes equations based on a staggered grid reveals good potential and allows for the first time the simulation of the whole flow field, from the conditions in the stagnation chamber to those in the flooded space. Its results provide a good representation of the main features of the flow, including the distribution of flow parameters not measured in the experiments. The algorithm is characterized by low implicit artificial viscosity and seems to be an effective tool for numerical simulation of the wide variety of problems concerning two-dimensional laminar compressible flows.

This work was partially supported by the Italian Space Agency (ASI). We acknowledge the support of a post doctoral fellowship for A. Broc by the European Space Agency and the support of PhD fellowship (M. Vigliotti) by Politecnico di Torino. A. Parodi is thanked for his valuable technical assistance. We are grateful to S. Ya. Khmel and E. A. Baranov (Institute of Thermophysics SB RAS, Russia) for their tests of the effect of the orifice on the nozzle wall in the throat region.

REFERENCES

Ashkenas, H. & Sherman, F. S. 1966 The structure and utilization of supersonic free jets in low density wind tunnels. *Proc. 4th Intl Symp. on Rarefied Gas Dynamics* (ed. J. H. De Leeuw), Vol. 2, pp. 84–105. Academic.

Bauer, H.-J. & Sahm, K. F. 1965 Relaxation of the vibrational, electronic, and rotational degrees of freedom of the NO molecule. *J. Chem. Phys.* **42**, 3400–3404.

Beylich, A. E. 1999 Structure and Applications of Jets. *Proc. 21th Intl Symp. on Rarefied Gas Dynamics* (ed. R. Brun, R. Campargue, R. Gatignol & J.-C. Lengrand), Vol. 1, pp. 553–566. Cépaduès Éditions, Toulouse, France.

Bird, G. A. 1994 *Molecular Gas Dynamics and the Direct Simulation of Gas Flows.* Clarendon Press, Oxford.

Boyd, I. D., Beattie, D. R. & Cappelli, M. A. 1994 Numerical and experimental investigations of low-density supersonic jets of hydrogen. *J. Fluid Mech.* **280**, 41–67.

Boyd, I. D., Chen, G. & Candler, G. V. 1995 Predicting failure of the continuum fluid equations in transitional hypersonic flows. *Phys. Fluids* **7**, 210–219.

Boyd, I. D., Penko, P. F., Meissner, D. L. &. DeWitt, K. J. 1992 Experimental and numerical investigations of low-density nozzle and plume flows of nitrogen. *AIAA J.* **30**, 2453–2461.

Brechignac, Ph., De Benedictis, S., Halberstadt, N., Withaker, B. K. 1985 Infrared-absorption and predissociation of NO dimer. *J. Chem. Phys.* **83**, 2064–2069.

Broc, A., Dilecce, G., Sharafutdinov, R. G., Skovorodko, P. A. & De Benedictis, S. 2001 Study of N_2 and O_2 plasma jet under continuous and pulsed rf discharge excitation: TALIF measurements of N and O atoms. *Proc. ISPC-15, Orleans* (ed. A. Bouchoule, J. M. Pouvesle, A. L. Thomann, J. M. Bauchire & E. Robert), Vol. 4, pp. 1285–1291.

Campbell, D. H., Wysong, I. J., Weaver, D. P. & Muntz, E. P. 1994 Flow-field characteristics in free jets of monoatomic and diatomic gases. *Proc. 18th Intl Symp. on Rarefied Gas Dynamics* (ed. B. D. Shizgal & D. P. Weaver). Progress in Astronautics and Aeronautics, Vol. 158, pp. 90–97. AIAA.

Chung, C. H., De Witt, K. J., Stubbs, R. M. & Penko, P. F. 1995 Simulation of overexpanded low-density nozzle plume flow. *AIAA J.* **33**, 1646–1650.

Cline, M. C. 1976 Computation of two-dimensional, viscous nozzle flow. *AIAA J.* **14**, 295–296.

De Bendictis, S. & Dilecce, G. 1995 Vibrational relaxation of N_2(C,v) state in N_2 pulsed RF discharge: electron impact and pooling reactions. *Chem. Phys.* **192**, 149–162.

De Benedictis, S., Dilecce, G. & Simek, M. 1999*a* Excitation and decay of $N_2(B^3\prod_g, v)$ states in pulsed discharge: kinetics of electrons and long-lived species. *J. Chem. Phys.* **110**, 2947–2961.

De Benedictis, S., Dilecce, G., Simek, M. &.Vigliotti, M 1998 Experimental study of N_2 RF plasma jet by optical methods. *Plasma Source Sci. Technol.* **7**, 557–571.

De Benedictis, S., Dilecce, G., Vigliotti, M., Marsilio, R. & Pandolfi, M. 1999*b* NO rotational temperature and density LIF measurements in a supersonic jet expansion. *Proc. ISPC-14, Prague* (ed. M. Hrabovský, M. Konrád & V. Kopecký), Vol. 2, pp. 619–624.

Dilecce, G., Simek, M., Vigliotti, M. & De Benedictis, S. 2000*a* Fast LIF approach to NO rotational temperature and density measurement: application to a gas-dynamic expansion. *Appl. Spectrosc.* **54**, 824–831.

Dilecce, G., Vigliotti, M. & De Benedictis, S. 2000*b* A TALIF calibration method for quantitative oxygen atom density measurement in plasma jets. *J. Phys.* D **33**, L53–L56.

Djakov, B. E., Enikov, R. & Oliver, D. 1997 Supersonic jets with periodic structure due to arc plasma expansion into low pressure ambient. *Contrib. Plasma Phys.* **37**, 57–76.

Djakov, B. E., Enikov, R., Oliver, D., Sicha, M., Novak, M., Soukup, L., Jastrabik, L. & Tichy, M. 1999 Plasma source producing supersonic plasma jets. *Proc. ISPC-14, Prague*, Vol. 2, pp. 631–636.

George, J. D. & Boyd, I. D. 1999 Simulation of nozzle plume flows using a combined CFD-DSMC approach. *AIAA Paper* 99-3454.

Gokhale, S. S. & Suresh, R. 1997 Numerical computations of internal flows for axisymmetric and two-dimensional nozzles. *Intl J. Numer. Meth. Fluids* **25**, 599–610.

Golomb, D. & Good, R. E. 1968 Clustering in isentropically expanding nitric oxide and their effect on the chemiluminous NO-O reaction. *J. Chem. Phys.* **19**, 4176–4180.

Harlow, F. H. & Welsh, J. E. 1965 Numerical calculation of time-dependent viscous incompressible flow of fluid with free surface. *Phys. Fluids* **8**, 2182–2189.

Hirschfelder, J. O., Curtiss, C. F. & Bird, R. B. 1954 *Molecular Theory of Gases and Liquids.* Wiley.

Holmes, R., Jones, G. R. & Lawrence, R. 1964 Rotational relaxation in carbon dioxide and nitrous oxide. *J. Chem. Phys.* **41**, 2955–2956.

Karsten, V. M., Sharafutdinov, R. G., Skovorodko, P. A. & Skrynnikov, A. V. 1999 Experimental investigation and direct simulation of flow in gasdynamic window. *Proc. 21th Intl Symp. on Rarefied Gas Dynamics* (ed. R. Brun, R. Campargue, R. Gatignol & J.-C. Lengrand), Vol. 1, pp. 655–662. Cépaduès Éditions, Toulouse, France.

Kim, S. C. 1994 Calculations of low-Reynolds-number resistojet nozzles. *J. Spacecraft Rockets* **31**, 259–264.

Korte, J. J. 1992 Aerodynamic design of axisymmetric hypersonic wind-tunnel nozzles using a least-squares/parabolized Navier-Stokes procedure. *J. Spacecraft Rockets* **29**, 685–691.

Lambert, J. D. 1977 *Vibrational and Rotational Relaxation in Gases.* Clarendon.

Maté, B., Graur, I. A., Elizarova, T., Shirokov, I., Tejeda, G., Fernández, J. M. & Montero, S. 2001 Experimental and numerical investigation of an axisymmetric supersonic jet. *J. Fluid Mech.* **426**, 177–197.

McKenzie, R. C. 1993 Progress in laser spectroscopy techniques for aerodynamic measurements: an overview. *AIAA J.* **31**, 465–477.

Murphy, H. R. & Miller, D. R. 1984 Effects of nozzle geometry on kinetics in free-jet expansion. *J. Phys. Chem.* **88**, 4474–4478.

O'Neil, C. & Brokaw, R. S. 1963 Relation between thermal conductivity and viscosity for nonpolar gases. II. Rotational relaxation of polyatomic molecules. *Phys. Fluids* **6**, 1675–1682.

Rae, W. J. 1971 Some numerical results on viscous low-density nozzle flows in the slender-channel approximation. *AIAA J.* **5**, 811–820.

Rebrov, A. K., Karelov, N. V., Sukhinin, G. I., Sharafutdinov, R. G. & Lengrand, J.-C. 1981 Electron beam diagnostics in nitrogen: secondary processes. *Proc. 12th Intl Symp. on Rarefied Gas Dynamics* (ed. S. S. Fisher), Progress in Astronautics and Aeronautics, Vol. 74, Part. II, pp. 931–945. AIAA.

Robin, L., Vervisch, P. & Cheron, B. G. 1994 Experimental study of a supersonic low-pressure nitrogen plasma jet. *Phys. Plasmas* **1**, 444–458.

Rosenhauer, M., Plähn, K. & Hannemann, K. 1999 Comparison of decoupled hybrid Navier–Stokes – DSMC calculations with experiments in plumes. *Proc. 21th Intl Symp. on Rarefied Gas Dynamics* (ed. R. Brun, R. Campargue, R. Gatignol & J.-C. Lengrand), Vol. 1, pp. 671–678. Cépaduès Éditions, Toulouse, France.

Rothe, D. E. 1971 Electron-beam studies of viscous flow in supersonic nozzles. *AIAA J.* **5**, 804–811.

Skovorodko, P. A. 1997 Nonequilibrium flow of gas mixture in supersonic nozzle and in free jet behind it. *Proc. 20th Intl Symp. on Rarefied Gas Dynamics* (ed. Ching Shen), pp. 579–584. Peking University Press, Beijing, China.

Yanenko, N. N. 1971 *The Method of Fractional Steps for Solving Multi-Dimensional Problems of Mathematical Physics in Several Variables.* Springer.

Zel'dovich, Ya. B. & Raizer, Yu. P. 1967 *Physics of Shock Waves and High-Temperature Hydrodynamic Phenomena.* Academic.